

Extreme Magnetic Field Modulus Variability of the Bp star HD 57372

S. Hubrig¹, S. D. Chojnowski², S. P. Järvinen¹, I. Ilyin¹, and K. Pan³

¹ Leibniz-Institut für Astrophysik Potsdam (AIP), An der Sternwarte 16, 14482 Potsdam, Germany
e-mail: shubrig@aip.de

² NASA Ames Research Center, Moffett Field, CA 94035, USA

³ Apache Point Observatory and New Mexico State University, P.O. Box 59, Sunspot, NM, 88349-0059, USA

Received MM DD, 2024; accepted MM DD, 202X

ABSTRACT

Context. In chemically peculiar Ap/Bp stars with large-scale organised magnetic fields with a simple centred dipole configuration, the ratio between the maximum and the minimum of the mean magnetic field modulus is of the order of 1.25. Values of 2 or more are observed only for very few Ap/Bp stars and are indicative of a very unusual magnetic field geometry.

Aims. Determining the magnetic field structure of Ap/Bp stars is bound to provide a different insight into the physics and the origin of the magnetic fields in early-type stars. In this respect, the Bp star HD 57372 is of particular interest because strongly variable magnetically split lines are observed in HARPS and APOGEE spectra.

Methods. We obtained and analysed measurements of the mean magnetic field modulus and of the mean longitudinal magnetic field using near-infrared spectra and optical polarimetric spectra distributed over the stellar rotation period.

Results. The mean magnetic field modulus $\langle B \rangle$ of HD 57372, as estimated from absorption lines that are split via the Zeeman effect and resolved in both optical and near-infrared spectra, is found to vary by an extraordinary amount of about 10 kG. The exceptional value of 3 for the ratio between the maximum and the minimum of the field modulus is indicative of a very unusual geometry of HD 57372's magnetic field. All observable quantities are found to vary in phase with the photometric period of 7.889 day. This includes the longitudinal magnetic field $\langle B_z \rangle$, which varies from -6 kG up to 1.7 kG in FORS2 spectra as well as the metal line strengths, whose equivalent widths change by up to 50% of their mean values over the course of the rotation period. The B8 temperature class of HD 57372 also places it among the hottest stars known to exhibit resolved, magnetically split lines.

Key words. stars: magnetic fields – stars: chemically peculiar – stars: early-type – stars: variables: general

1. Introduction

For well over 50 years it has been known that a significant fraction of late-B and A type stars host strong, large-scale magnetic fields that lead to peculiar surface abundances and hence also to their classification as chemically peculiar (CP) Ap/Bp stars (Babcock 1958). These stars are slow rotators as a rule when compared to their non-magnetic analogues, and in the most extreme cases of slow rotation, strong magnetic fields, and the presence of magnetically sensitive spectral lines, it is possible to resolve the individual magnetically split components in unpolarized light. Measurement of the wavelength separations of the split components combined with knowledge of the associated quantum numbers gives a very simple yet extremely valuable measure of the intrinsic surface magnetic field strength as averaged over the visible hemisphere, a quantity known as the magnetic field modulus ($\langle B \rangle$; see Mathys 1990a; Mathys & Lanz 1992; Mathys et al. 1997; Mathys 2017). For all other magnetic stars, diagnosis of the intrinsic magnetic field strength usually relies on spectropolarimetric observations of circular polarization over the full rotation period.

The first example of resolved, magnetically split lines (RMSL) in an Ap/Bp star was HD 215441 (more commonly known as Babcock's Star; Babcock 1960), and despite more than a hundred additional examples having subsequently been found, Babcock's Star remains unique to this day. Not only is it the most magnetic main sequence star known ($\langle B \rangle \sim 34$ kG), it is a relatively rapid rotator (compared to most RMSL stars) and also

the hottest star for which RMSL have been observed. In particular, Preston (1969) used time series $\langle B \rangle$ measurement to confirm that the 9.49 days photometric period found by Jarzembowski (1960) was in fact the rotational period (P_{rot}) of Babcock's Star, and based on the strength of temperature sensitive features in the spectra, he concluded that the temperature class could be as hot as B3 or B4.

In contrast to Babcock's Star, the majority of Ap/Bp stars known to exhibit RMSL have far longer rotation periods. For example, the 29 year rotation of HD 50169 could only be determined after a few decades of observation (Mathys et al. 2019), and the rotation period of HD 101065 (also known as Przybylski's Star; Przybylski 1961) could only be constrained to ~ 188 years by Hubrig et al. (2018) despite an even longer observational baseline. With early/mid-A spectral types, typical RMSL stars are also cooler than Babcock's Star, and with $\langle B \rangle$ usually less than 10 kG, they are also considerably less magnetic (Mathys 2017).

The most comprehensive studies of RMSL stars to date have been provided by Mathys (2017) in particular essentially providing an encyclopedia on the magnetic properties of what at the time was an 84-star sample. Among the key findings of this work was confirmation of an already-suspected dearth of short-period binaries among the RMSL stars, leading to the suspicion that the peculiarities of these stars may stem from binary mergers. In lieu of a theory for generating magnetic fields in a purely radiative atmosphere, the binary merger hypothesis is a promising one that

has only recently gained traction to the point where a theoretical basis is now being developed (e.g. Schneider et al. 2020).

For numerous RMSL stars, both the $\langle B \rangle$ and the brightnesses of the stars vary as a function of rotation phase due to the changing viewing angle of the magnetic poles, such that rotation periods can be determined from either photometry or spectroscopy. These variations can often be successfully reproduced under the assumption of a simple dipole using the framework developed by Preston (1969) in his study of Babcock’s Star, whereby the ratio of $q = \langle B \rangle_{\max} / \langle B \rangle_{\min}$ should be of the order of 1.25 in the case of a pure dipole. For some of the RMSL stars however, the magnetic field geometry is clearly more complicated. Out of a subset of 28 RMSL stars with known rotation periods over which $\langle B \rangle$ had been measured, Mathys (2017) found eight stars with $q > 1.25$, six of which had $q > 1.3$. Among these six stars, the A3p star HD 65339 stood out as exceptionally remarkable considering $P_{\text{rot}} = 8.03$ days, $q \sim 2.27$, and $\Delta_{\langle B \rangle} = \langle B \rangle_{\max} - \langle B \rangle_{\min} \sim 9.7$ kG (see also Mathys et al. 1997). In terms of $\Delta_{\langle B \rangle}$, the only fair comparison currently known is the A2p star HD 126515, for which $\Delta_{\langle B \rangle} \sim 6$ kG, albeit it over a much longer timescale of $P_{\text{rot}} \sim 130$ days.

In the context of q , it is worth mentioning HR 465, which has long been known as one of the most extreme Bp stars in respect to its exotic atomic line content (e.g. Cowley et al. 1975), complicated variability over its long ~ 21 year rotation period (Scholz 1978), and an unprecedentedly large $q \sim 3.8$ (Mathys et al. 1997; Giarrusso et al. 2022). As with Babcock’s Star, HR 465 is thus a severe outlier among the RMSL stars, though in this case representing the extreme low end of all measured magnetic field moduli, with $\langle B \rangle < 3$ kG on average.

Here, we present a new example of a RMSL Bp star whose magnetic properties are every bit as exceptional as those of Ap stars such as HD 65339 and HR 465. Prior to this work, HD 57372 had not been specifically mentioned in any papers beyond inclusion in the Bernhard et al. (2015) search for photometric variability in CP stars. These authors reported a V -band magnitude that varies between 7.90–7.93 over the course of a 7.888 day period. The B8p Si spectral type, indicating enhanced Si features in the optical, was reported in the catalog of CP stars by Renson & Manfroid (2009).

Four medium-resolution H -band spectra of HD 57372 have been obtained by the northern Apache Point Observatory Galactic Evolution Experiment (APOGEE; Majewski et al. 2017; Wilson et al. 2019) spectrograph, which operates as a sub-component of fifth instalment of the Sloan Digital Sky Survey (SDSS-V; e.g. Ahumada et al. 2020, and Kollmeier, J.A., in preparation). Intriguingly, our inspection of these spectra shows extreme short-term variability of RMSL. To investigate HD 57372 in more detail, we acquired eight high-resolution polarimetric spectra from the High Accuracy Radial Velocity Planet Searcher (HARPS; Pepe et al. 2000; Mayor et al. 2003) instrument attached to the European Southern Observatory (ESO) 3.6 m telescope and twelve low-resolution polarimetric spectra from the FOcal Reducer/low dispersion Spectrograph 2 (FOR2) mounted on the 8.2-m Antu unit of the Very Large Telescope (VLT). Further, numerous observations of HD 57372 by the Transiting Exoplanet Survey Satellite (TESS; Ricker et al. 2015) are also available, and we make use of them for refining the rotation period.

The paper is laid out as follows. Section 2 describes the spectroscopic and photometric data including the TESS lightcurve and associated refinement of P_{rot} . In Section 3 we discuss the Gaia DR3 parameters and in Section 4 the magnetic field variability of HD 57372 in both the optical and the near-infrared

(NIR) H -band is presented. In Section 5 we explore stellar parameters assessed based on the Balmer line $H\delta$ and surface abundances of HD 57372 in comparison to other magnetic Ap/Bp stars. Finally, in Section 6, we compare HD 57372 with Ap/Bp stars known to exhibit magnetically resolved lines and discuss its magnetic field structure.

2. Spectroscopy and photometry

2.1. SDSS 2.5m/APOGEE

HD 57372 was observed by the APOGEE spectrograph on the Sloan 2.5-m telescope (Gunn et al. 2006) at Apache Point Observatory (APO) four times over the course of a week between 2020 December 29 and 2021 January 6. The spectra have a resolution of about 22 500 and cover most of the H -band (15145–16960 Å; vacuum wavelengths used throughout this paper when referring to the H -band) onto three detectors, with gaps between 15800–15860 Å and 16430–16480 Å due to non-overlapping wavelength coverage of the detectors. Total exposure times ranged from 49 to 82 minutes, and the associated signal-to-noise ratios (S/N) range from 230 to 264. The reduction was carried out using the standard APOGEE data reduction pipeline described in Nidever et al. (2015), with the only post-reduction steps being continuum normalization via fitting low-order polynomials to line-free regions, correction of the wavelengths to rest frame based on Gaussian fitting of narrow absorption lines, and manual removal of otherwise distracting airglow emission residuals. When analysing individual absorption lines, we also re-normalised the local continuum in small regions enclosing the lines.

2.2. ESO 3.6m/HARPSpol

HD 57372 was observed with HARPS in the spectropolarimetric mode eight times between 2022 April 23 and 2022 May 1. In the spectropolarimetric mode of the HARPS has a resolving power of about 115 000 and a wavelength coverage from 3780 to 6910 Å, with a small gap between 5259 and 5337 Å. The data was reduced on La Silla using the HARPS data reduction pipeline. The normalization of the spectra to the continuum level is described in detail by Hubrig et al. (2013).

2.3. VLT 8m/FORS2

Twelve spectropolarimetric observations of HD 57372 have been obtained in service mode using FOR2 at the spectral resolution of about 2 000 between 2021 November 24 and 2022 April 1. The data reduction and analysis methods used for $\langle B_z \rangle$ measurement were described in detail in numerous previous papers (e.g., Schöller et al. 2017; Chojnowski et al. 2022) and will not be repeated here. As in those papers, the FOR2 data yielded two $\langle B_z \rangle$ data sets for the magnetic field measurements: one using only the hydrogen Balmer series lines ($\langle B_z \rangle_{\text{hyd}}$) and another using the entire spectrum from each observation ($\langle B_z \rangle_{\text{all}}$).

2.4. TESS lightcurve and rotation period

HD 57372 was observed 1086 times in TESS Sector 7 (120 s cadence) between 2019 January 8 and 2019 February 1, 3485 times in TESS Sector 33 (600 s cadence) between 2020 December 18 and 2021 January 13, 3474 times in TESS Sector 34 (600 s cadence) between 2021 January 14 and 2021 February 8, and

Table 1. Summary of the spectroscopic observations of HD 57372.

UT-Mid	JD-Mid 2.4E6+	Inst.	t_{exp} [s]	S/N	ϕ_{rot}
2020-12-29T07:56:09	59212.831	A	4899	240	0.3610
2021-01-03T07:40:17	59217.820	A	3919	259	0.9934
2021-01-04T07:48:46	59218.826	A	3919	230	0.1209
2021-01-06T07:57:01	59220.831	A	2939	264	0.3752
2022-04-23T23:48:11	59693.492	H	3600	115	0.2879
2022-04-24T23:47:23	59694.491	H	3600	111	0.4146
2022-04-25T23:35:26	59695.483	H	3600	117	0.5403
2022-04-27T23:30:03	59697.479	H	3600	116	0.7933
2022-04-29T00:06:04	59698.504	H	3600	95	0.9233
2022-04-29T23:24:50	59699.476	H	3600	92	0.0464
2022-05-01T00:33:06	59700.523	H	3600	137	0.1792
2022-05-02T00:23:28	59701.516	H	3600	105	0.3051
2021-11-24T06:53:34	59542.787	F	8×104	2735	0.1851
2022-01-10T01:28:33	59589.561	F	8×104	2266	0.1141
2022-01-12T01:26:32	59591.560	F	8×104	2992	0.3674
2022-01-18T07:18:20	59597.804	F	8×104	2305	0.1589
2022-02-04T01:50:44	59614.577	F	8×104	2345	0.2849
2022-02-16T03:02:18	59626.627	F	8×104	2938	0.8123
2022-03-13T04:45:24	59651.698	F	8×104	2352	0.9903
2022-03-14T05:00:23	59652.709	F	8×104	2536	0.1184
2022-03-22T01:31:43	59660.564	F	8×104	1905	0.1141
2022-03-23T03:47:31	59661.658	F	8×104	2491	0.2528
2022-03-31T01:13:26	59669.551	F	8×104	2188	0.2533
2022-04-01T01:11:34	59670.550	F	8×104	2626	0.3798

Notes: In the Inst. column, A stands for APOGEE, H stands for HARPS, and F stands for FORS2. HARPS S/N values were estimated at 5500 Å and APOGEE S/N values were estimated at 16000 Å.

10654 times in TESS Sector 61 (200 s cadence) between 2023 January 18 and 2023 February 12, bringing the grand total to just over 100 days of TESS exposure time spread out over 18,699 individual observations. We used the LIGHTCURVE (Lightcurve Collaboration et al. 2018) code to download the simple aperture photometry, to which a pixel mask accounting for blending with neighbour stars has been applied. After removing systematic trends and outliers via the TESSCUT code (Brasseur et al. 2019), we were left with a total of 18,064 TESS data points. The lightcurves from each sector are shown in the upper panels of Figure 1.

Analysis of the TESS data with the time series software package PERIOD04 (Lenz & Breger 2005) indicates a primary frequency of $f = 0.12675795 \pm 2.1 \times 10^{-7}$, which corresponds to a rotation period of $P_{\text{rot}} = 7.889148 \pm 1.3 \times 10^{-5}$. This result agrees well with what has been found in past studies, albeit with far greater precision. In the bottom panel of Figure 1, all of the TESS data has been phase folded by P_{rot} using 2458492.07 as a JD of maximum brightness. As is common for Ap/Bp stars (e.g. Jagelka et al. 2019) due to inhomogeneous elemental abundances and magnetic field strengths across their surfaces, the lightcurve of HD 57372 is quite irregular. Each rotation of HD 57372 witnesses two local brightness minima at $\phi \sim 0.32$ and ~ 0.72 that enclose a local brightness maximum roughly halfway between at $\phi \sim 0.52$.

With rotation phases (ϕ_{rot}) in hand, Table 1 summarises the spectroscopic observations of HD 57372, providing Universal Times (UT) at mid-exposure, Julian dates (JD) at mid-exposure minus 2400000, instruments used, exposure times, signal-to-noise ratios (S/N), and ϕ_{rot} .

3. Gaia DR3 parameters and radial velocity measurements

Although HD 57372 appears to be a single star in the 2MASS and DSS images provided on the HD 57372 SIMBAD page, the star has been identified as a visual double star in past studies. For example, the Tycho Double Star Catalogue (Fabricius et al. 2002) reported a component separation of $\sim 2''$, with the brighter component having magnitudes of $B_T = 8.15$ and $V_T = 8.30$ and with the fainter component having $B_T = 9.05$ and $V_T = 9.11$. The third data release of the Gaia mission (Gaia DR3; Gaia Collaboration et al. 2016, 2022) also reported two sources within $2''$ of HD 57372, one with $G = 8.289$ and one with $G = 9.121$. The Gaia DR3 parallaxes and proper motions of the brighter star ($\pi = 2.412$ mas, $\mu_\alpha = -7.928$ mas yr $^{-1}$, $\mu_\delta = 4.130$ mas yr $^{-1}$) are quite similar to those of the fainter star ($\pi = 2.378$ mas, $\mu_\alpha = -8.592$ mas yr $^{-1}$, $\mu_\delta = 4.263$ mas yr $^{-1}$) such that it is possible the two stars are physically associated. In this case, the orbital period will of the order of several thousand years. Spectroscopic parameters were only given for the fainter star. These included a radial velocity of $v_r = 24.63$ km s $^{-1}$ as well as an effective temperature of $T_{\text{eff}} = 13963$ K that is in good agreement with the B8 temperature class quoted for HD 57372 in the Renson & Manfroid (2009) catalogue of CP stars.

The radial velocity reported by Gaia for the fainter component of HD 57372 is quite close to the values we find from the APOGEE and HARPS spectra of the brighter, magnetic component. For the radial velocity measurements using the APOGEE H -band spectra of HD 57372 we relied on the Mg II 16765 Å, Ca II 16654 Å, Ce III 15961 Å, and Ce III 16133 Å lines. These are among the strongest identified lines covered, and their entire

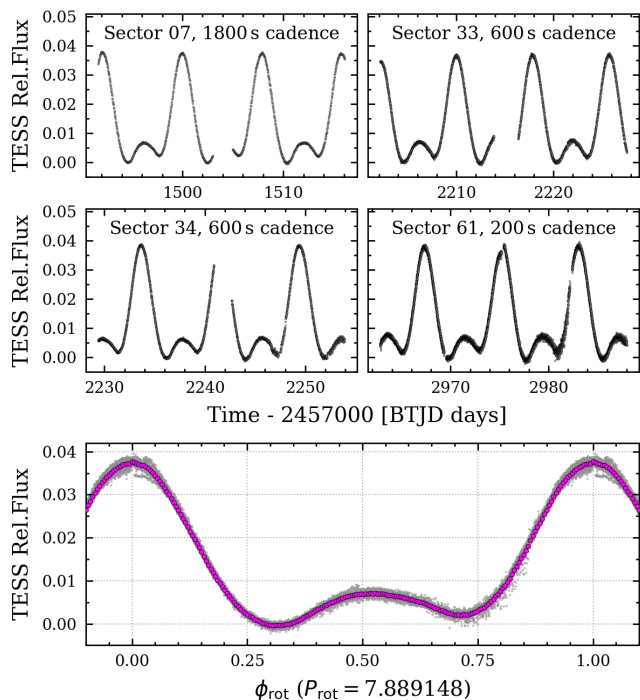


Fig. 1. TESS lightcurve of HD 57372. The upper panels show the observed data from each of four TESS sectors. Grey points in the lower panel are all of the data phased by the 7.889148 d rotation period and with 2458492.07 being a reference epoch of maximum brightness. Magenta points show the data binned in increments of $\phi_{\text{rot}} = 0.005$.

profiles could be satisfactorily fit with single Gaussians during epochs when the magnetic field strength was relatively low such that the magnetic splitting was not resolved. In the spectra where magnetic splitting was resolved, we fitted Gaussians to the central components of the quasi-triplet features of the Ca II and Ce III, discarding the Mg II line due to its distorted, non-triplet morphology. Barycentric velocity corrections were applied to the resulting averages of each spectrum, and the standard deviations of the line-by-line measurements were adopted as error estimates. This yielded an overall average of $v_r = 21.88 \pm 2.80 \text{ km s}^{-1}$ across the four APOGEE spectra, with individual v_r ranging from 21.30–22.87 km s^{-1} . From this, we have no reason to suspect that HD 57372 is a member of a binary system, or at least not of a short period binary.

In the HARPS optical spectra, v_r was measured similarly using Cr II and Fe II lines. The lines were selected on the basis of relatively short wavelengths ($< 4800 \text{ \AA}$) and relatively low effective Landé factors ($g_{\text{eff}} < 0.7$), to minimise the effects of magnetic splitting. This yielded an overall average of $v_r = 22.45 \pm 0.86 \text{ km s}^{-1}$ across the eight HARPS spectra, with individual v_r ranging from 21.63–23.51 km s^{-1} . The surprisingly large v_r scatter here seems to be caused by an inhomogeneous chemical element distribution on the stellar surface typically observed in Ap/Bp stars and a complicated magnetic field geometry rather than by binarity. However, our attempts to phase the individual v_r values with the rotation period did not show any conclusive correlation.

Although the Gaia data does not indicate the fainter component of HD 57372 being variable, the brighter component is classified as a photometric variable with a 7.888 d period. Considering that this is in good agreement with the rotation period of the magnetic component of HD 57372 indicated by our data, and also considering the aforementioned radial velocity agreement,

we proceed here under the assumption that the aforementioned Gaia DR3 spectroscopic parameters (including also the surface gravity of $\log g = 4.399$ and the stellar radius of $R_* = 1.88 R_{\odot}$) in fact pertain to the Bp star HD 57372 that is the focus of this paper. Assuming that the TESS 7.889 d period is in fact the rotation period of HD 57372, then the $R_* = 1.88 R_{\odot}$ would imply a rotational velocity at the equator $v_{\text{eq}} = 12 \text{ km s}^{-1}$.

The relatively small angular separation of the two objects may lead to contamination of the primary spectrum by the secondary. The APOGEE fibers subtend $2''$ on the sky, whereas the HARPS fibers have a diameter of $1''$, and the used FORS2 slit was $0.4''$. Therefore, for the APOGEE observations we expect that some light of the secondary was captured. For HARPS and FORS2, contamination will be rather small. However, we do not see any evidence for a second star in our data. Further, as we show in the following sections, all observables vary according to a rotation period that can be independently measured from photometry, Zeeman splitting variability, line strength variability, and longitudinal field variability, confirming that they are tied to one single star. All results presented in our paper are typical for a single magnetic star, albeit an extreme one.

4. Magnetic field measurements

4.1. H-band variability of the magnetic field modulus

We present in the upper panel of Figure 2 line identifications in the H-band spectra of HD 57372. As is typical for late-Bp stars, the hydrogen Brackett series are the strongest features in the spectra, while the metal line content is dominated by the rare earth ion Ce III along with singly-ionized elements such as Mg II, Si II, and Ca II. We also show in the spectrum of HD 57372 most of the unidentified lines that were previously discussed by Chojnowski et al. (2019, 2020, 2023). These features have no likely counterparts in the existing atomic data.

The lower panel of Figure 2 highlights the remarkable variability of spectral lines over the course of one week. Whereas the $\phi_{\text{rot}} = 0.361$ and 0.375 spectra show hardly any evidence of magnetic splitting, most of the lines are clearly split by a strong magnetic field during the $\phi_{\text{rot}} = 0.121$ and 0.993 spectra. The best examples of this are Ca II 16654 \AA and Ce III 16133 \AA , both of which have quasi-triplet Zeeman patterns.

Atomic transitions in which the upper and lower energy levels both have total angular momentum quantum numbers equal to 0.5 (i.e. $J_1 = J_2 = 0.5$) but only one of the levels is split (i.e. with a non-zero Landé factor, $g_1 = 0, g_2 > 0$ or $g_1 > 0, g_2 = 0$) are known as Zeeman doublets. In absence of the partial Paschen-Back effect, which should not have too strong impact at the modest field strengths in question, this combination of J and g values leads to a Zeeman pattern consisting of two π components, each of which overlaps in wavelength or velocity space with a corresponding σ component. In these cases, the mean magnetic field modulus can be estimated via $\langle B \rangle (\text{G}) = \Delta\lambda / (k g \lambda_0^2)$ (Mathys et al. 1997) where g is the Landé factor of the split level, k is a constant equal to $4.671 \times 10^{-13} \text{ kG}^{-1} \text{ \AA}^{-1}$, λ_0 is the rest wavelength of the transition in units of \AA , and $\Delta\lambda$ is the separation of the Zeeman doublet components in units of \AA . For a pure Zeeman triplet, g is either the Landé factor of the split level of the transition, if the other level is unsplit, or if the transition is between two split levels that have the same Landé factor, the value of the latter.

No such transitions are present in the H-band spectra of HD 57372, so in order to estimate $\langle B \rangle$ from the Zeeman quasi-triplet features that are present, we replace g with the effective

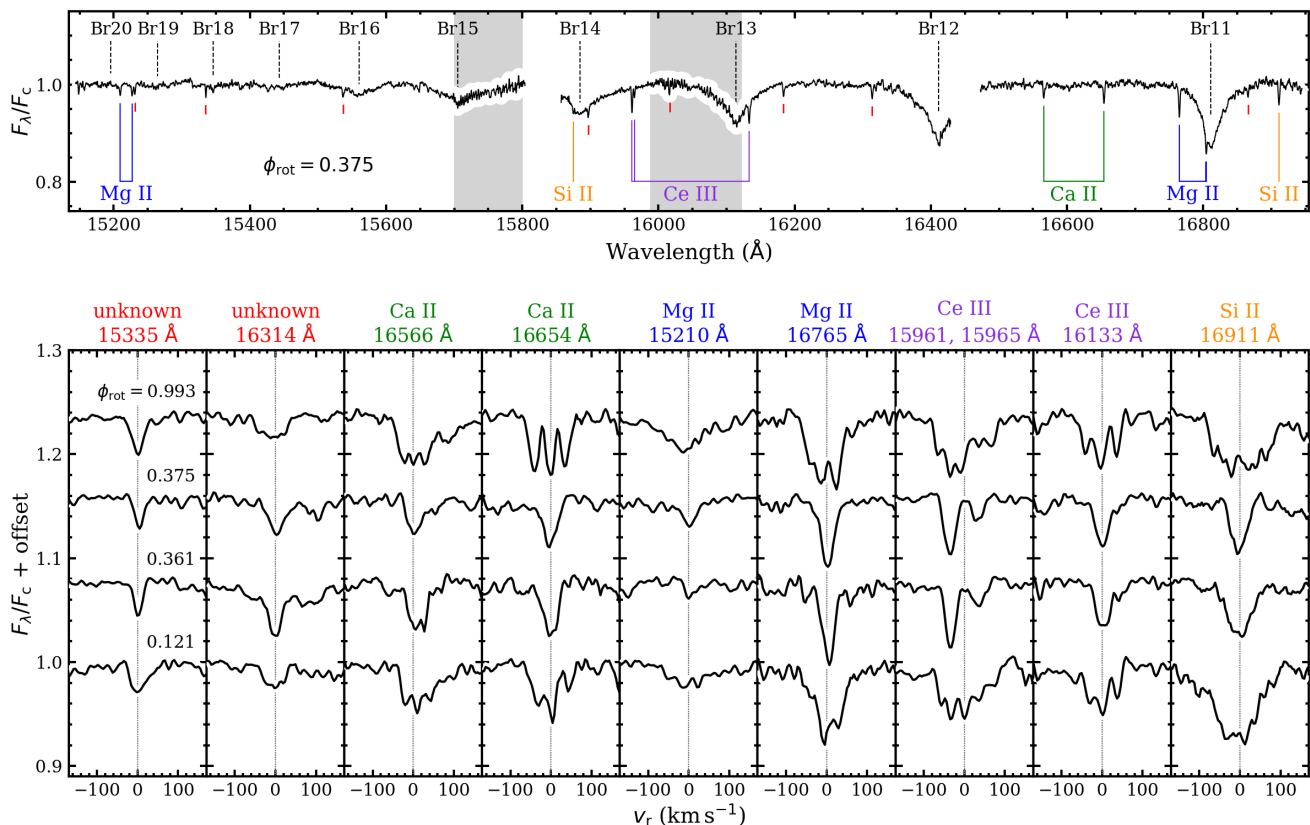


Fig. 2. *Upper panel:* line identifications in the APOGEE spectrum of HD 57372 at the rotational phase $\phi_{\text{rot}} = 0.375$. The hydrogen Brackett series lines are labelled along the top, while metal lines are labelled along the bottom. Unidentified lines are indicated by small red ticks below the spectrum. *Lower panel:* variability of individual lines as a function of ϕ_{rot} .

Landé factors (g_{eff} ; see equation 4 of Mathys 1990b) of the transitions and $\Delta\lambda$ with half of the separation of the outer triplet components. This makes it straightforward to estimate $\langle B \rangle$ from the $\phi_{\text{rot}} = 0.121$ and 0.993 APOGEE spectra of HD 57372. The most cleanly split lines in these spectra are Ca II 16654 Å and Ce III 16133 Å, and from them we find $\langle B \rangle \sim 14.5$ kG at $\phi_{\text{rot}} = 0.121$ and ~ 15.3 kG at $\phi_{\text{rot}} = 0.993$.

The question now is, how low is $\langle B \rangle$ during the $\phi_{\text{rot}} = 0.361$ and $\phi_{\text{rot}} = 0.375$ spectra? Figure 3 represents our attempt to answer this question. We have yet to see resolved magnetic splitting in the unknown line at 15335 Å in the APOGEE spectra of any star, meaning that it has a quite low g_{eff} and thus is relatively insensitive to the magnetic field. The 15335 Å line is by far the narrowest line in the APOGEE spectra of HD 57372, and it has an observed minimum FWHM of ~ 21 km s $^{-1}$ in the $\phi_{\text{rot}} = 0.361$ spectrum. To demonstrate this, a Gaussian of this FWHM has been plotted over the 15335 Å line profiles.

In the Ca II 16654 Å and Ce III 16133 Å panels of Figure 3, we have assumed that ~ 21 km s $^{-1}$ is roughly the intrinsic FWHM in the absence of a magnetic field, and we have also approximated the Zeeman patterns as simple ensembles of three Gaussians with fixed FWHM = 21 km s $^{-1}$. The positions and depths of the individual Gaussians have then been adjusted manually in order to arrive at the displayed results. Although the quoted $\langle B \rangle$ values are highly uncertain during the $\phi_{\text{rot}} = 0.361$ and 0.365 spectra, the implication is that $\langle B \rangle$ has dropped below 6 kG and hence that $\langle B \rangle$ changes by nearly 10 kG over the course of each rotation cycle.

It is worth noting the high degree of asymmetry of the line profiles in the $\phi_{\text{rot}} = 0.121$ spectrum. This is atypical of the

APOGEE-observed Ap/Bp stars that exhibit RMSL, and is likely due to the rotational Doppler shifts of the contributions to the observed, disc-integrated lines coming from different parts of the stellar disc.

4.2. Optical variability of the magnetic field modulus

Before discussing the rich line content of the optical HARPS spectra of HD 57372, we repeated with the HARPS spectra the exercise detailed in the previous subsection for estimating $\langle B \rangle$ though in this case making use of Zeeman doublet features. Similar to the APOGEE spectra, RMSL are observed in numerous lines in half of the HARPS spectra while $\langle B \rangle$ was too weak for any RMSL to be observed in the other half. The middle and righthand panels of Figure 4 show the two best available Zeeman doublet features – Fe II 6149 Å ($g = 2.70$) and Si II 6699 Å ($g = 2.67$). Several other doublets such as Ti II 4315 Å ($g = 2.63$) and Fe II 4385 Å ($g = 2.68$) are also covered by the HARPS spectra, but we focus on the longer wavelength lines since blending is far more of a concern in the 4300 Å region and because the Zeeman splitting is larger for a fixed g or g_{eff} as wavelength increases.

Also shown in Figure 4 is Fe II 4491 Å, which is the best available of a magnetically insensitive ($g_{\text{eff}} = 0.43$) line that shows no resolved splitting in any of the HD 57372 spectra. Whereas lines with $g_{\text{eff}} = 0$ (e.g. Fe I 5434 Å) are often present in the optical spectra of Ap stars, HD 57372 is sufficiently hot that Fe I lines are very weak or not present. During the low- $\langle B \rangle$ HARPS spectra, the Fe II 4491 Å has an observed FWHM of roughly 16 km s $^{-1}$. Taking into account unresolved splitting

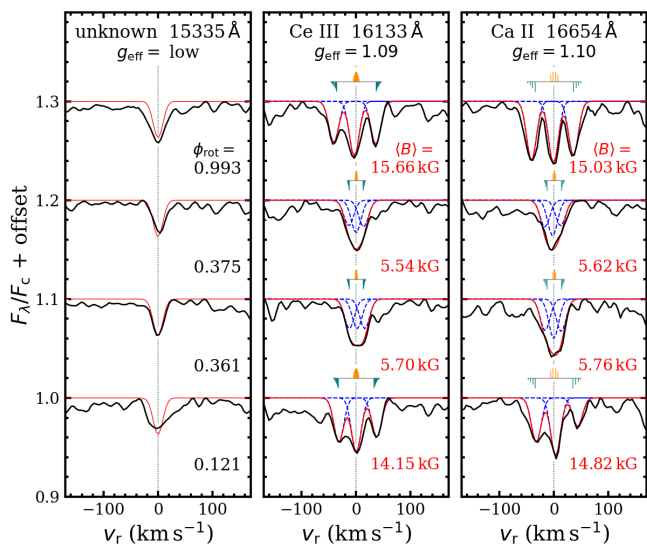


Fig. 3. Mean magnetic field modulus estimates from the Ce III 16133 Å and Ca II 16654 Å lines in the APOGEE *H*-band spectra. The relatively magnetically insensitive unknown line at 15335 Å is shown in order to demonstrate that it is well fit by a single Gaussian with FWHM= 21 km s⁻¹ during the low- $\langle B \rangle$ epochs. For Ce III 16133 Å and Ca II 16654 Å, the triple Gaussians each have the same FWHM= 21 km s⁻¹. The associated $\langle B \rangle$ estimates are given below each line profile, but it is important to note that the low- $\langle B \rangle$ values are highly uncertain due to the magnetic splitting being unresolved at APOGEE’s resolution

that will slightly broaden the line, the Gaussian used to fit this line shown in Figure 4 has a fixed FWHM= 14 km s⁻¹.

As can be seen in this figure, the Si II 6699 Å line, provides a satisfactory fit to the magnetically split doublet components during the low- and high- ϕ_{rot} phases where the splitting is resolved. In the case of Fe II 6149 Å however, which is the most frequently used $\langle B \rangle$ diagnostic since it is present and relatively strong for the majority of Ap stars (Mathys 2017), the splitting is during all epochs contaminated by one or more unknown features such that a simple double Gaussian composite is insufficient for a satisfactory fit. The presence of the Si II 6699 Å line, on the other hand, requires quite severe Si enhancement, and not only is this the case for HD 57372, the line is quite isolated with no likely contaminants in the vicinity. Our placement of the Fe II 6149 Å double Gaussians in Figure 4 was therefore guided by what is shown for Si II 6699 Å, which we regard as the ground truth in this case.

It is important to note that no algorithmic fitting occurred in the creation of Figures 3 and 4. Rather, the positions and depths of the Gaussians were all adjusted manually in order to achieve qualitative best fits. These plots are useful for guiding the eye, but they do not provide formal errors. The level of uncertainty is clearly quite high between $\phi_{\text{rot}} = 0.2$ – 0.7 given that magnetic splitting was unresolved in the associated spectra.

Even in the spectra where the splitting was resolved, the behaviour of the splitting is quite different with respect to most RMSL stars for three reasons. First, in all of the HARPS spectra of HD 57372 that exhibit RMSL, there is a high degree of asymmetry in the depths of the low- and high-velocity Zeeman components. At low ϕ_{rot} , the high velocity components are shallower than the low velocity components, and the depths of the shallower components diminish as ϕ_{rot} increases. Second, the positions of the components appear to drift towards higher velocity

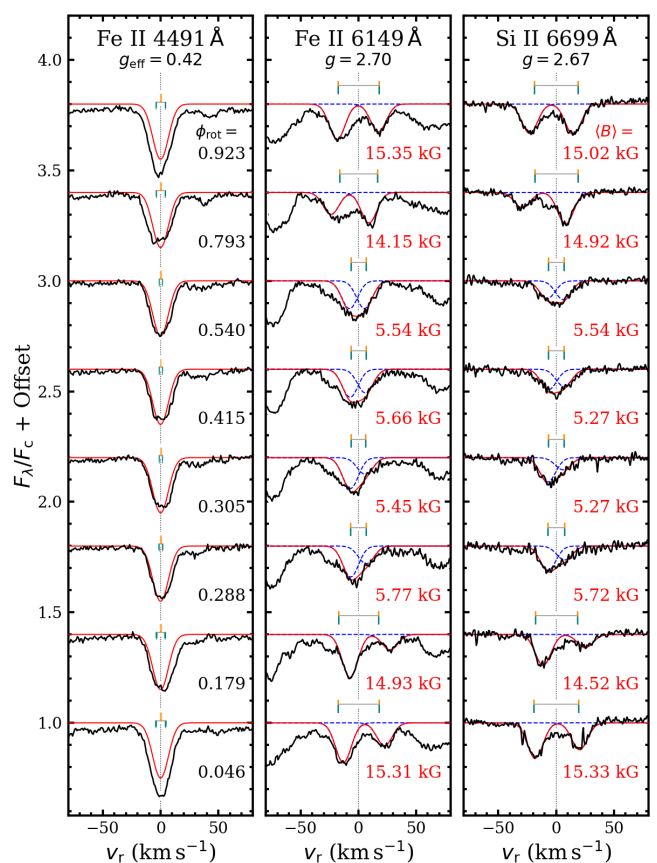


Fig. 4. Similar to Figure 3 but for the HARPS optical spectra. As in that figure, the best available magnetically insensitive line (Fe II 4491 Å) is also shown, and the displayed Gaussians for the lines Fe II 6149 Å and Si II 6699 Å have fixed FWHM=16 km s⁻¹. This value is based on the Si II 6699 Å, where it gives the best fit to the magnetically split doublet components at e.g. rotation phases 0.046, 0.793, and 0.923. The Gaussian used to fit the line Fe II 4491 Å has a fixed FWHM= 14 km s⁻¹. Its depth has been fixed to match the observed depth in the $\phi_{\text{rot}} = 0.540$ spectrum.

as ϕ_{rot} increase from $\phi_{\text{rot}} = 0$. These behaviours then appear to reverse at some intermediate ϕ_{rot} , such that the mirror image occurs as ϕ_{rot} approaches unity. Third, the observed line profiles of the unblended, pure Zeeman doublet Si II 6699 Å line cannot be accounted for with a simple two Gaussian composite during any of the ϕ_{rot} extrema spectra. On the other hand, there is no reason to expect the shapes of the split components to be Gaussian, as even for very slowly rotating stars, they depend on the distribution of the magnetic field strength over the visible stellar disk. Given the non-negligible value of the projected equatorial velocity, the shape difference between the blue and red components of the Fe II and Si II doublets in HD 57372 reflects the different combinations of Zeeman and Doppler effects on different parts of the stellar surface. The similar behaviour of the Fe II and Si II doublet lines considered here strengthens this interpretation, even though part of the component difference in Fe II must also result from partial Paschen-Back effect.

4.3. Longitudinal magnetic field

4.3.1. HARPS observations

As we have done in our previous studies using HARPSpol data (see, e.g. Järvinen et al. 2020), we employed the least-squares

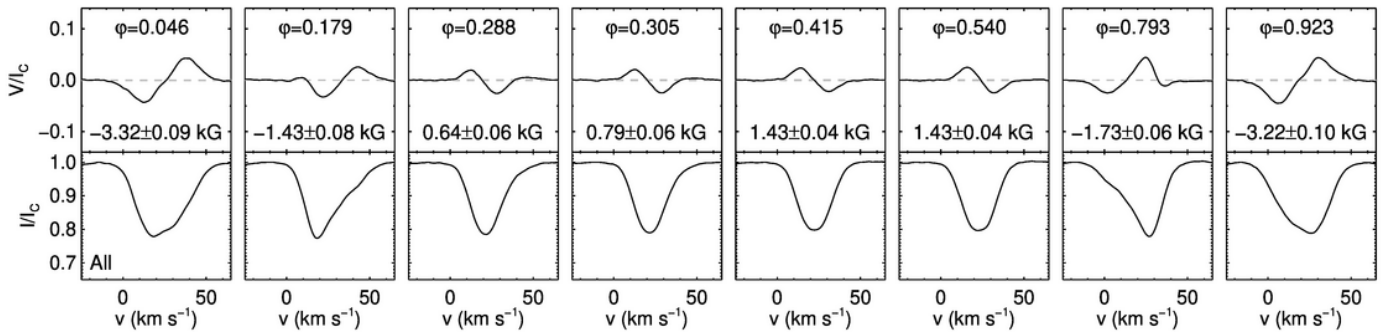


Fig. 5. LSD Stokes I (bottom), and Stokes V (top) calculated using HARPS spectropolarimetric observations of HD 57372 recorded on different rotation phases. The employed line mask includes all identified spectral lines that appear to be unblended or minimally blended. The rotational phases and the measured longitudinal magnetic field strengths are presented on the top. The dashed lines in the Stokes V panels indicate the mean uncertainties, which for the presented line mask are of the order of the thickness of these lines.

Table 2. Radial velocity and magnetic field measurements.

Inst.	ϕ_{rot}	v_r [km s $^{-1}$]	$\langle B \rangle$		$\langle B \rangle$ Ca II 16654 [kG]	$\langle B_z \rangle$ all [kG]	$\langle B_z \rangle$ hydrogen [kG]
			Si II 6699 [kG]	Ce III 16133 [kG]			
H	0.046	23.14±0.74	15.33			-3.32±0.09	
F	0.114					-4.40±0.08	-3.66±0.10
F	0.114					-4.31±0.08	-3.63±0.09
F	0.118					-4.26±0.08	-3.59±0.08
A	0.121	21.71±3.22		14.15	14.82		
F	0.159					-3.00±0.07	-2.61±0.10
H	0.179	22.49±1.04	14.47			-1.43±0.08	
F	0.185					-2.12±0.14	-1.66±0.18
F	0.253					-0.08±0.04	-0.03±0.07
F	0.253					-0.07±0.04	-0.03±0.07
F	0.285					0.74±0.04	0.72±0.07
H	0.288	21.81±0.55	5.72			0.64±0.06	
H	0.305	21.63±0.55	5.27			0.79±0.06	
A	0.361	21.30±2.67		5.70	5.76		
F	0.367					1.72±0.09	1.65±0.10
A	0.375	21.64±2.74		5.54	5.62		
F	0.380					1.70±0.04	1.65±0.05
H	0.415	21.70±0.46	5.23			1.43±0.04	
H	0.540	22.31±0.76	5.54			1.43±0.04	
H	0.793	22.98±1.33	14.92			-1.73±0.06	
F	0.812					-3.29±0.07	-2.74±0.09
H	0.923	23.51±1.06	15.02			-3.22±0.10	
F	0.990					-6.05±0.09	-5.25±0.10
A	0.993	22.87±2.53		15.66	15.03		

Notes: Instrument column meanings are as in Table 1. In the $\langle B_z \rangle$ met/all column, HARPS values pertain to $\langle B_z \rangle$ as measured from apparently unblended metal lines while FORS2 values pertain to $\langle B_z \rangle$ as measured from the full spectra.

deconvolution (LSD) technique following the description given by Donati et al. (1997) in order to increase the accuracy of the mean longitudinal magnetic field ($\langle B_z \rangle$) determination on different rotation phases. The parameters of the lines used to calculate the LSD profiles were taken from the Vienna Atomic Line Database (VALD3; Kupka et al. 2011). Only lines that appear to be unblended or minimally blended in the Stokes I spectra were included in the line mask. The resulting profiles are scaled according to the line strength and sensitivity to the magnetic field. The final line mask contains 87 lines and includes Si, Ti, Cr, Fe, and Sr lines, also lines belonging to the rare-earth element (REE group such as Nd, Dy, and Er). The LSD profiles calculated with this line mask are shown in Fig. 5. Since the diagnostic null polarization spectrum calculated according to the definition

of Donati et al. (1997) is featureless and perfectly flat, it is not presented in this figure. The mean longitudinal magnetic field is usually determined by computing the first-order moment of the LSD Stokes V profile according to Mathys (1989).

Further, as numerous studies of Ap/Bp stars in the past have revealed that different elements typically show different abundance distributions across the stellar surface, we carried out LSD magnetic field measurements using line masks for each element separately. These previous studies also indicated a kind of symmetry between the topology of the magnetic field and the element distribution. Thus, the structure of the magnetic field can be potentially studied by measurements of the magnetic field using spectral lines of each element separately. In Fig. A.1 we present the measurements of the longitudinal magnetic field us-

ing line masks containing Ti II, Cr II, Fe II, and Sr II lines, whereas Fig. A.2 shows the results for twice ionised REE elements Dy III, Er III, and Nd III. Additionally, we present in Fig. A.3 magnetic field measurements carried out separately for Si II and Si III lines to check the presence of an anomalies related to the vertical abundance stratification frequently observed in Ap/Bp stars (e.g. Hubrig et al. 2018). The measured mean longitudinal magnetic field strengths for all line masks are presented in Table A.1.

The presence of a magnetic field in the LSD profile is evaluated according to Donati et al. (1992), who define that a Zeeman profile with a false alarm probability (FAP) $\leq 10^{-5}$ is considered as a definite detection, $10^{-5} < \text{FAP} \leq 10^{-3}$ as a marginal detection, and $\text{FAP} > 10^{-3}$ as a non-detection. All used line masks for all eight epochs give definite detections.

The general behaviour of the mean longitudinal magnetic field strength calculated for all masks is rather similar: the field is positive throughout observed rotation phases 0.288–0.540 and negative in the phases 0.793–0.179. For the field calculated using the line mask with all 87 spectral lines the strongest negative field (-3.32 ± 0.09 kG) is measured around the phase 0, whereas the strongest positive field (1.43 ± 0.04 kG) is detected around the phase 0.5. The observed single change of the field polarity hints at a prevailing dipolar field structure. The LSD Stokes I profiles presented in Fig. 5 appear asymmetric when the field has negative polarity, indicating the presence of an inhomogeneous element surface distribution and are almost symmetric when the field shows positive polarity.

The longitudinal magnetic field strengths measured using Sr II and the iron-peak elements Ti II, Cr II, and Fe II show a very similar behaviour. The strongest field of negative polarity is measured around the phase 0: Ti II lines give the strongest field of -3.68 ± 0.18 kG followed by Cr II and Fe II whereas using Sr II lines the field is clearly weaker with the strength of -2.51 ± 0.43 kG. Ti II lines show the strongest positive field of 1.82 ± 0.08 kG at the phase 0.540. The positive magnetic longitudinal magnetic field measured using Sr II LSD profiles shows maximum field strength at phase the 0.288. The presence of asymmetric Stokes I profiles in the phases with the negative field indicate surface inhomogeneous abundance distribution of these elements.

Interestingly, the longitudinal magnetic fields of negative polarity measured using different REE line masks (Fig. A.2) appear to be much stronger than fields measured using other elements. This can be explained that, similar to several previous studies of Ap and Bp stars, these elements are distributed on the stellar surface closer to the location of the magnetic pole of negative polarity (e.g., Hubrig et al. 2018; Järvinen et al. 2020). The measurements using Dy III lines account for -5.56 ± 0.40 kG and those for Nd III and Er III are around -4 kG. On the other hand, the positive longitudinal magnetic field strengths for REEs are comparable with those obtained for iron peak elements. The Stokes I profiles exhibit a distinct structure in all rotation phases, indicating a surface inhomogeneous abundance distribution.

We do not find any indication for the presence of a vertical stratification of Si: the line profiles using both Si II and Si III lines are very similar. Also the measured longitudinal fields do not differ much apart from the negative field extrema with $\langle B_z \rangle = -3.25 \pm 0.15$ kG measure for Si II lines and $\langle B_z \rangle = -2.28 \pm 0.09$ kG for Si III lines. Otherwise magnetic fields measured using both line lists follow the common pattern being most negative around the phase 0 and most positive around phase 0.5.

4.3.2. FORS2 observations

Twelve FORS2 spectropolarimetric observations of HD 57372 were obtained in service mode over a few months from 2021 to 2022. Unfortunately, a few observations cover similar rotation phases, e.g. around the phases 0.1, 0.25, and 0.37, implying larger gaps in the rotation phase coverage between 0.38 and 0.81, and 0.81 and 0.99. The measurements of the mean longitudinal magnetic field were carried out using procedures presented in prior work (e.g., Hubrig et al. 2004a,b; Schöller et al. 2017). The obtained longitudinal magnetic field strengths using for the measurements only the hydrogen Balmer series lines ($\langle B_z \rangle_{\text{hyd}}$) and using the entire spectrum ($\langle B_z \rangle_{\text{all}}$) present clear rotational modulation, which is expected for a large-scale organised dipole field structure and show change of polarity, with the strongest mean longitudinal magnetic field of negative polarity $\langle B_z \rangle_{\text{all}} = -6.05 \pm 0.09$ kG in the rotation phase 0.990 and the strongest field of positive polarity $\langle B_z \rangle_{\text{all}} = 1.72 \pm 0.09$ kG in the rotation phase 0.367.

In Table 2 we present, along with the radial velocity measurements reported in Sect. 3, our magnetic field measurements using all NIR and optical observations at our disposal, acquired with different instruments. Photometric, spectroscopic, and magnetic variability of HD 57372 as a function of rotation phase is presented in Fig. 6. All measurements show a good correlation with the TESS light curve exhibiting stronger (in absolute values) mean magnetic field moduli, mean longitudinal magnetic fields, and line profile intensities of the studied elements in rotational phases around the light curve maximum. Remarkably, equivalent widths change by up to 50% of their mean values over the course of a rotation period.

5. Atmospheric parameters and abundances

Our visual inspection of the available high-resolution spectra of HD 57372 suggests that this star, similar to other magnetic Ap/Bp stars, is extreme in abundances of several elements. In order to estimate the stellar parameters and surface abundances of HD 57372, we created a small grid of synthetic spectra using the SYNTH program with ATLAS9 model atmospheres (Kurucz 2005) and the VALD atomic linelist. To minimise the impact of magnetic broadening, we focussed our analysis on the average of the four HARPS spectra taken during intermediate rotational phases when no magnetic splitting is observed ($\phi_{\text{rot}} = 0.288, 0.305, 0.415, 0.540$). The rotational velocity was fixed to $v \sin i = 14 \text{ km s}^{-1}$ based on the width of Fe II 4491 Å, which as previously noted is one of the least magnetically sensitive lines present in the spectra. The microturbulent velocity was fixed to 2 km s^{-1} .

The effective temperature (T_{eff}) and surface gravity ($\log g$) were assessed based on the Balmer series lines with some consideration given to the behaviour of metal lines, for example the weakness of the Fe I lines and the strength of the Fe III lines. Whereas neutral helium is a good T_{eff} diagnostic for normal late-B stars, it is usually found to be depleted on the surfaces of late-Bp stars like HD 57372. A total of 78 synthetic spectra were created, with T_{eff} ranging from 11500–15000 K in steps of 500 K and with $\log g$ ranging from 3.7–4.5 in steps of 0.1 dex. The left panel of Figure 7 shows some of the synthetic spectra that provide a reasonable match to the H δ line of HD 57372.

Although the model spectrum with $T_{\text{eff}} = 12500$ K and $\log g = 3.8$ provides a good fit to the cores of the Balmer series lines, it is important to note a few following aspects. First, the optical spectra of HD 57372 contain a plethora of lines with no

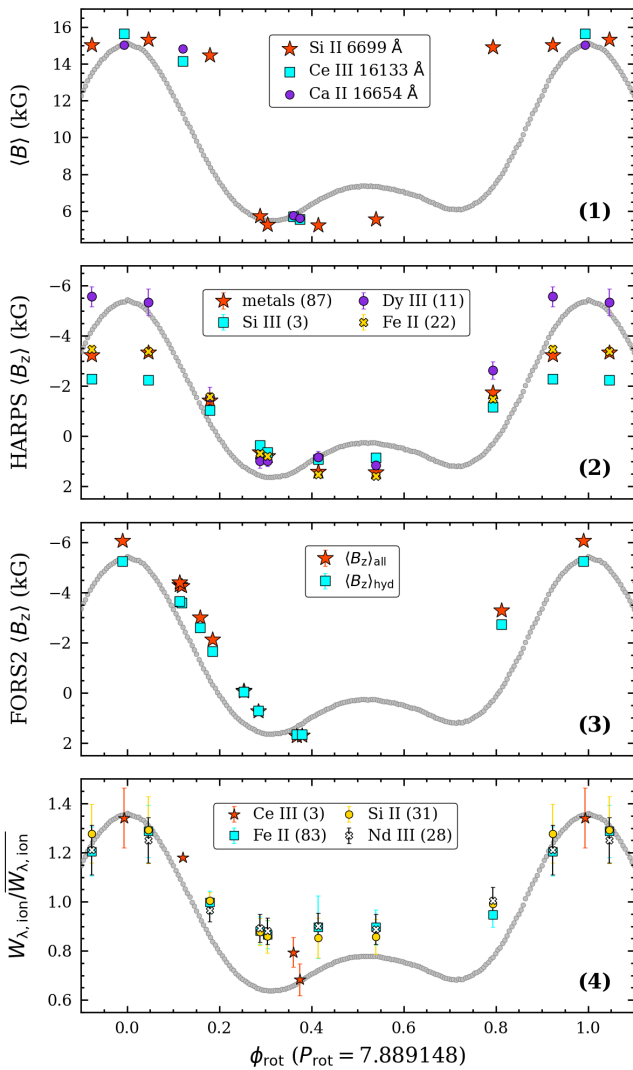


Fig. 6. Variability of HD 57372 as a function of rotation phase. The phase-binned TESS lightcurve (magenta points in Figure 1) is shown as grey points in each panel. The ordinate scaling of the lightcurve is similar to that of the bottom panel of Figure 1, but the associated y-axis tick labels have been omitted to emphasize the units of the scatter points. Panel (1) shows the $\langle B \rangle$ estimates from the Si II 6699 Å line in the HARPS spectra and from the Ce III 16133 Å and Ca II 16654 Å lines in the APOGEE spectra. Panel (2) shows the HARPS $\langle B_z \rangle$ measurements, including those obtained from numerous metal lines, from three Si III lines, from 11 Dy III lines, and from 22 Fe II lines. These ions were selected simply to demonstrate the larger degree of scatter in $\langle B_z \rangle$ when $\langle B \rangle$ is high. Panel (3) shows the $\langle B_z \rangle$ measurements from the FORS2 data, including those from the full spectra and those from the hydrogen lines. Panel (4) shows the equivalent width variations for four example ions, with the numbers of lines averaged for each ion given in parentheses.

reasonable counterparts in the available atomic data. It is therefore reasonable to expect the depths of the hydrogen lines to be blanketed to some extent. Second, while Si I and Fe I are all but absent from the observed spectra, lines from Si II, Si III, Fe II, and Fe III are plentiful. Adoption of $T_{\text{eff}} = 12500$ K results not only in neutral Si and Fe lines that are far too strong, but also in large discrepancies between the singly-ionized versus doubly-ionized abundances of Si and Fe.

As for the hotter model spectra, those with $T_{\text{eff}} \geq 14000$ K are disfavoured due to the poor fits to the cores of the Balmer

Table 3. Abundance estimates from the mean low- $\langle B \rangle$ HARPS spectrum of HD 57372.

Atom/ion	Z	[X/H] (dex)	N
He I	2.00	-0.05 ± 0.02	1
C II	6.01	0.81 ± 0.05	3
N II	7.01	1.41 ± 0.38	6
O I	8.00	1.00 ± 0.14	3
O II	8.01	1.73 ± 0.11	5
Ne I	10.00	0.35 ± 0.19	4
Mg II	12.01	0.96 ± 0.20	10
Al II	13.01	0.73 ± 0.16	5
Al III	13.02	1.52 ± 0.16	5
Si II	14.01	1.83 ± 0.28	36
Si III	14.02	2.63 ± 0.05	4
P II	15.01	0.80 ± 0.04	2
S II	16.01	1.42 ± 0.24	33
Cl II	17.01	3.14 ± 0.35	27
Ca II	20.01	1.92 ± 0.25	9
Sc II	21.01	2.13 ± 0.12	5
Ti II	22.01	2.16 ± 0.29	38
V II	23.01	0.86 ± 0.06	2
Cr II	24.01	1.71 ± 0.24	34
Mn II	25.01	0.76 ± 0.00	2
Fe II	26.01	1.61 ± 0.18	64
Fe III	26.02	2.09 ± 0.22	9
Co II	27.01	1.92 ± 0.06	2
Ni II	28.01	0.47 ± 0.34	2
Sr II	38.01	2.94 ± 0.04	2
Ce III	58.02	3.84 ± 0.08	2
Pr III	59.02	3.87 ± 0.14	3
Nd III	60.02	4.09 ± 0.20	28
Tb III	65.02	3.94 ± 0.36	7
Dy III	66.02	3.96 ± 0.35	19
Ho III	67.02	3.59 ± 0.05	3
Er III	68.02	4.13 ± 0.20	8

Notes: The abundances are given relative to the solar abundances presented by Asplund et al. (2021). The number of spectral lines used for the abundance determination is presented in the last column.

lines. We thus conclude that the T_{eff} of HD 57372 is likely in the range 12500–14500 K and that the $\log g$ is likely in the range 3.8–4.2, and proceed to estimate abundances for the case of $T_{\text{eff}} = 13500$ K and $\log g = 4.0$. Due to the aforementioned prevalence of unknown lines in the spectra of HD 57372 as well as the inevitable effects of magnetic broadening, even during the low- $\langle B \rangle$ epochs, we used the equivalent width (W_λ) matching technique in order to derive abundances.

The vast majority of identifiable lines in the observed spectra can be attributed to Fe II, so we began by estimating the iron abundance based on 78 lines that appeared to be minimally blended. For each line, the continuum normalization was adjusted in 300 km s^{-1} windows centred on the rest wavelengths and W_λ was then measured via direct flux integration in fixed 20 km s^{-1} windows centred on the rest wavelengths. The same procedure was then applied to synthetic spectra, with $[\text{Fe}/\text{H}]$ being adjusted until the synthetic W_λ matched the observed W_λ . Obvious outliers (mostly due to blending with unknown lines) were then rejected, and the line-by-line abundances were averaged. A total of 64 lines yielded $[\text{Fe}^+/\text{H}] = 1.610 \pm 0.182$. From visual inspection, it was clear that the doubly-ionized iron abundance did not agree with that of singly-ionized iron, so the Fe III

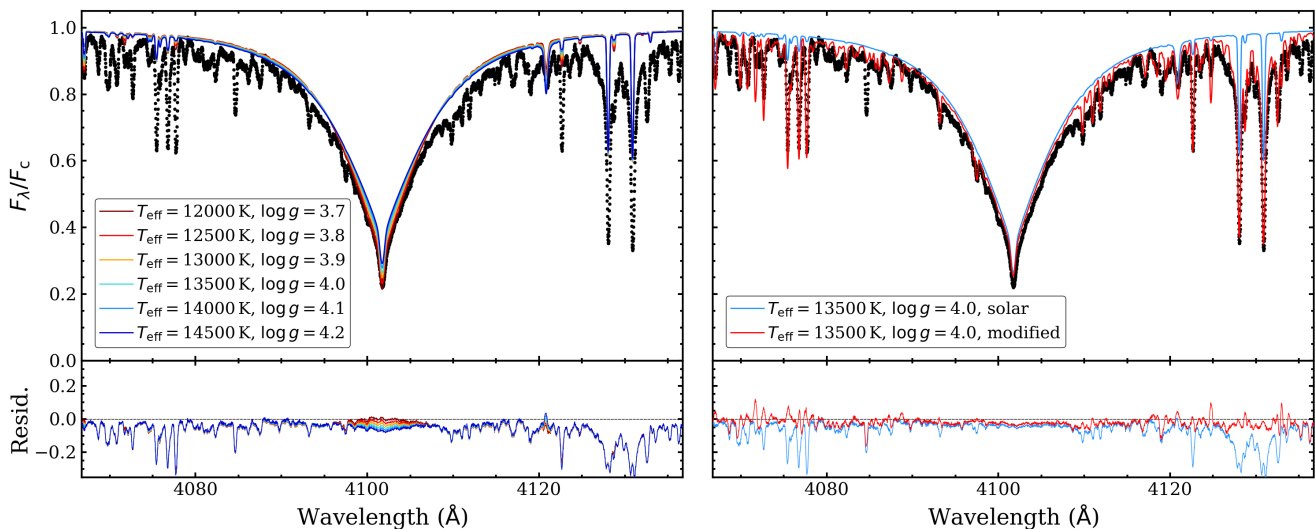


Fig. 7. *Left:* Comparison of the observed H δ line (black dots) from the mean low- $\langle B \rangle$ spectrum of HD 57372 to solar abundance synthetic spectra (coloured curves) covering a range of T_{eff} and $\log g$. *Right:* Similar to the left panel, but now with the blue curve showing the solar abundance synthetic spectrum with the adopted $T_{\text{eff}} = 13500 \text{ K}$ and $\log g = 4.0$, and with the red curve being the same but with abundances adjusted as quoted in Table 3.

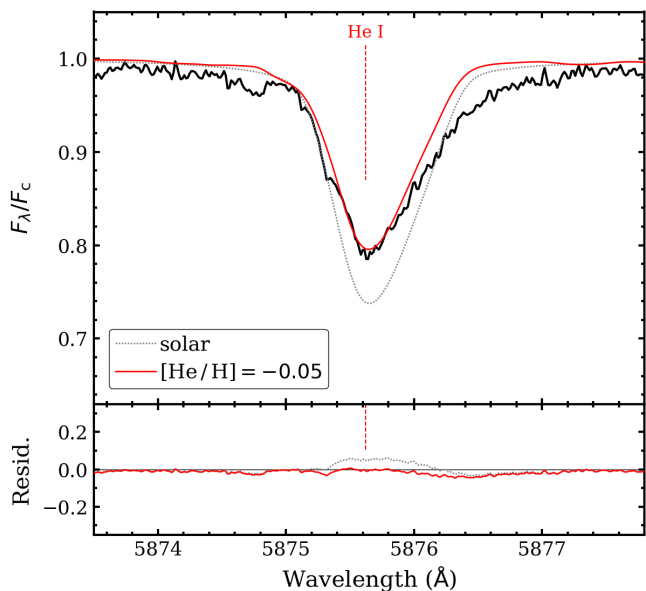


Fig. 8. Estimate of the helium abundance from the He I 5875 \AA line for the case of $T_{\text{eff}} = 13500 \text{ K}$ and $\log g = 4.0$. The dotted line is a synthetic spectrum with solar helium abundance while the solid red line has a decreased helium abundance. Observed minus synthetic residuals are shown in the low panel.

abundance was estimated independently in the same manner using an initial list of nine lines that appeared to be free of blending with Fe II. This yielded $[\text{Fe}^{++}/\text{H}] = 2.089 \pm 0.222$ from a total of nine lines. All subsequent abundance estimates were carried with fixed $[\text{Fe}/\text{H}] = 1.610$.

The next strongest and most numerous contributions to the observed spectra beyond iron include Ti II, Si II, S II, and Cr II. We proceeded over these elements iteratively by first estimating the Ti II abundance and keeping it constant for subsequent abundance estimates, then estimating the Si II abundance and keeping it constant for subsequent abundance estimates, and so on for a total of 31 ions that we are confident contribute to the observed spectra. The only exceptions to this general process were oxy-

gen, silicon, and aluminum, for which both singly-ionized and doubly-ionized lines are present. Similar to the case of iron, the abundances of different ionization stages were estimated independently for these elements. In the right panel of Figure 7 we show a good fit of the observed H δ line by the atmosphere model with abundances adjusted as quoted in Table 3.

With some noteworthy exceptions, the trend in the abundance results presented in Table 3 is generally similar to those of the majority of Ap/Bp stars whose abundances have been previously estimated (e.g. Ghazaryan et al. 2018). As is demonstrated in Figure 8, helium is clearly depleted with respect to solar. This is a common feature of Ap/Bp stars photospheres, as is the strong enhancement of silicon, iron peak elements, and strontium, and the very strong enhancement of rare earth elements. However, one element certainly sticks out due to its remarkable overabundance: we detect a strong chlorine enhancement of 3.14 dex above solar. It appears to be stronger than ever reported for any Ap/Bp star in the past, albeit with just six stars in the literature for which chlorine abundances have been reported. Our estimate of the ionised chlorine abundance using three different synthetic spectra is presented in Figure 9.

6. Discussion

HD 57372 possesses a very strong magnetic field, with an exceptionally large amplitude of variation of the magnetic field modulus of about 10 kG over the rotation period of 7.889 d. The maximal strength of $\langle B \rangle = 15.66 \text{ kG}$ is measured using the Zeeman triplet Ce III 16133 \AA and the lowest $\langle B \rangle = 5.23 \text{ kG}$ is estimated using the Zeeman doublet Si II 6699 \AA . All observable quantities are found to vary in phase. This includes the longitudinal magnetic field $\langle B_z \rangle$, which varies in FORS2 spectra from roughly -6 kG up to $+1.7 \text{ kG}$, as well as the metal line strengths, whose equivalent widths change by up to 50% of their mean values over the course of a rotation period. In the high-resolution spectra recorded in visual and NIR spectra, we detect significant variability of the line profiles over the rotation cycle. We also observe in Stokes I spectra significant distortion of the resolved components of the Zeeman doublets Si II 6699 \AA and

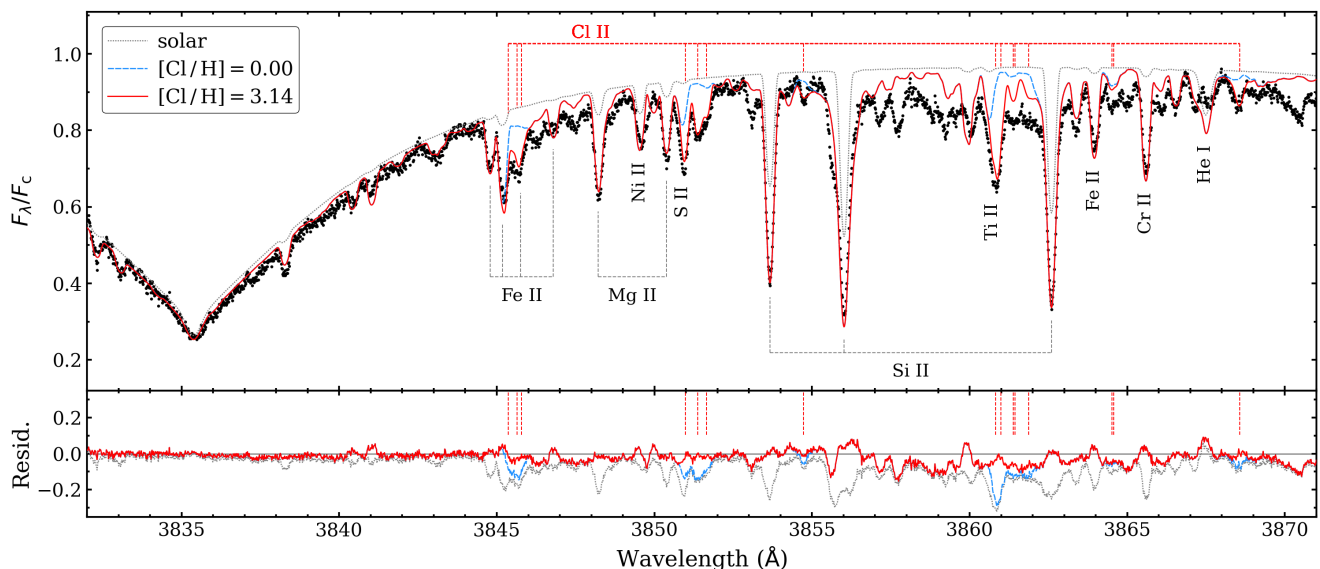


Fig. 9. Estimate of the ionised chlorine abundance. The observed spectrum is shown as black dots. As indicated in the legend, three synthetic spectra are shown. The dotted grey curve has solar abundances across the board and the dashed blue curve has all abundances except for Cl adjusted to the values given in Table 3. The solid red curve is then the same as blue except for $[\text{Cl}^+/\text{H}]$ having been increased by 3.14 dex.

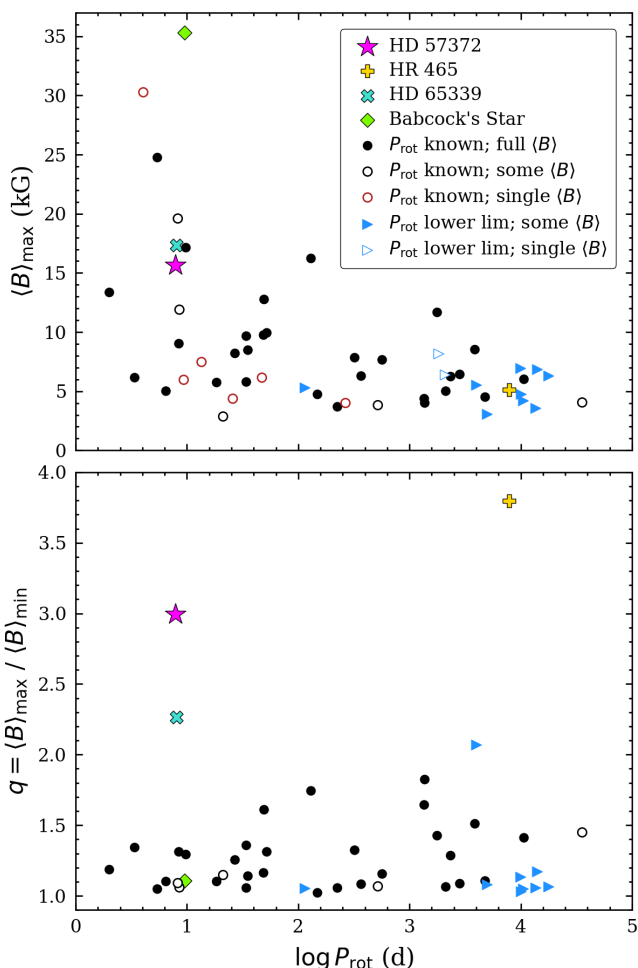


Fig. 10. Comparison of HD 57372 to other stars known to exhibit resolved, magnetically split lines in the optical. *Upper panel:* the maximum or only available $\langle B \rangle$ estimate as a function of P_{rot} . *Lower panel:* the ratio of $\langle B \rangle_{\text{max}}$ over $\langle B \rangle_{\text{min}}$ as a function of P_{rot} . In both panels, some of the more exceptional stars are indicated by their own symbol and colour.

Fe II 6149 Å. Such distortions are most likely due to the combination of different amounts of Doppler and Zeeman effects on different parts of the stellar surface covered by chemical spots.

The exceptional value of 3 of the ratio between the maximum and the minimum of the mean magnetic field modulus that is observed in this Bp star is indicative of a very unusual geometry of its magnetic field. In Fig. 10 we compare HD 57372 to other Ap/Bp stars known to exhibit resolved, magnetically split lines in the optical. Most of the measurements were provided by Mathys et al. (1997), Elkin et al. (2012), Mathys (2017, and references therein), and Giarrusso et al. (2022). In the top panel of this figure we present the maximum or only available $\langle B \rangle$ estimates as a function of P_{rot} . Only a handful of other stars show stronger $\langle B \rangle$ than HD 57372. The distribution of the ratio q of the maximum to the minimum of the mean magnetic field modulus measured in HD 57372 is presented in the bottom of Fig. 10 along with the ratio of $\langle B \rangle_{\text{max}}$ over $\langle B \rangle_{\text{min}}$ for other Ap/Bp stars as a function of P_{rot} . Among the presented stars, only HR 465 shows a stronger value for the ratio q , of the order of 3.8 (Mathys et al. 1997; Giarrusso et al. 2022), with the second strongest ratio of about 2.3 determined for HD 65339 (Mathys et al. 1997). It is of interest that the magnetic field of the Ap star HD 65339 with the rotation period of 8.03 d (Mathys 2017, and references therein) shows a complex structure with the best fit of the $\langle B \rangle$ variation curve using the superposition of a cosine wave and of its first harmonic (e.g. Mathys 2017, and references therein). As for the Bp star HR 465 with a very long rotation period of about 22.7 yr (Mathys 2017, and references therein), Giarrusso et al. (2022) conclude that its magnetic field structure should show some significant departure from a centred dipole. Inspecting figure 4 in Giarrusso et al. (2022), we note that the shapes of the $\langle B \rangle$ phase curves of both stars, HR 465 and HD 57372, show similarly broad, fairly flat minima and sharper-peaked maxima.

Our longitudinal magnetic field measurements show just one change of polarity, suggesting that the field topology of HD 57372 is predominantly dipolar. For Ap/Bp stars, it is quite common to see variations of the strength of their magnetic field. These variations can easily be described by the oblique rotator model, which was introduced by Stibbs (1950). The stellar mag-

netic field is rotating with the star and one can see different aspects of it. The oblique rotator assumes a dipolar magnetic field tilted with the obliquity angle β with respect to the rotation axis, which itself is inclined with respect to the line-of-sight by the angle i . In the cases that i is zero, one is looking at the rotation pole and no modulation of the magnetic field with rotation can be seen. The same is true in cases of $\beta = 0$, i.e. the magnetic field axis is aligned with the rotation axis.

Using this model, the inclination angle i between the rotation axis of the star and the line of sight is usually constrained if the rotation period and the stellar radius R are known and from the measurements of $v \sin i$. In Sect. 3 we reported $v_{eq} = 12 \text{ km s}^{-1}$ using Gaia DR3 determinations $\log g = 4.399$ and the stellar radius of $R_* = 1.88 R_\odot$) and assuming the TESS photometric period of 7.889 d. On the other hand, we adopted somewhat different stellar parameters, $T_{\text{eff}} = 13500 \text{ K}$ and $\log g = 4.0$, in Sect. 5 to achieve a better match to the H δ line of HD 57372. The lower values for $\log g$ and T_{eff} imply a slightly larger stellar radius and therefore a larger equator velocity v_{eq} , which, however, can not be greater than 14 km s^{-1} estimated in Sect. 4.2 using the magnetically weakly sensitive Fe II 4491 Å line with the relatively low effective Landé factor $g_{\text{eff}} = 0.43$. The implication of the finding that the values for equator velocity and the projected rotation velocity $v \sin i$ are nearly the same is that the inclination angle i between the rotation axis of the star and the line of sight is close to 90° . However, for this angle, we would expect equal field strength for both negative and positive poles, whereas our magnetic field measurements show a much stronger field of negative polarity.

In the following we assume the inclination angle $i = 85 \pm 5^\circ$ to test whether it is still possible to describe the magnetic field structure of HD 57372 by a simple dipolar field geometry. The general description for the strength of the observed longitudinal magnetic field for a simple centred dipole was presented by Preston (1967):

$$\langle B_z \rangle = \frac{1}{20} \frac{15 + u}{3 - u} B_d (\cos \beta \cos i + \sin \beta \sin i \cos 2\pi t/P) \quad (1)$$

with $\langle B_z \rangle$ the effective magnetic field, β the angle between the rotation axis and the magnetic axis, i the angle between the rotation axis and the line of sight, P the rotation period of the star, u the limb-darkening coefficient and B_d the strength of the dipolar magnetic field.

The relative amplitude of variation of the longitudinal field is usually characterised by the parameter r representing the ratio between $B_{z,\text{min}}$ and $B_{z,\text{max}}$. In our case with $B_{z,\text{max}} = -6.0 \pm 0.1 \text{ kG}$ and $B_{z,\text{min}} = 1.7 \pm 0.1 \text{ kG}$ measured in FORS2 spectra using the entire spectra we calculate $r = -3.53 \pm 0.22$. Using the formula

$$r = \frac{B_{z,\text{min}}}{B_{z,\text{max}}} = \frac{\cos \beta \cos i - \sin \beta \sin i}{\cos \beta \cos i + \sin \beta \sin i} \quad (2)$$

we calculate a very small obliquity angle $\beta = 8.90 \pm 8.81^\circ$. With the limb-darkening coefficient of 0.4 (Claret 2019) we obtain an incredibly strong and implausible polar magnetic field strength of $B_d = -84 \pm 52 \text{ kG}$. It is not clear whether the exceptional structure of the magnetic field in HD 57372 is related to the unusually high field strength or to the presence of significant departures of its magnetic field from the simple centred dipole magnetic field geometry.

On the other hand, given the poor phase coverage, in particular between the rotation phases 0.2 and 0.8 where the field modulus becomes smaller and the longitudinal field measurements

indicate positive polarity, our assumption of sinusoidal field variability may be wrong. Obviously, additional high-resolution spectroscopic and polarimetric observations with a more dense coverage of the rotation cycle are necessary to better constrain the phase curves for the mean field modulus and the mean longitudinal field that can be in fact anharmonic with noticeable deviations from a sinusoid. In our observations, the $\langle B \rangle$ maximum coincides with the negative longitudinal magnetic field $\langle B_z \rangle_{\text{all}}$ extrema measured in HARPS and FORS2 spectra, while the $\langle B \rangle$ minimum is found close in phase with positive longitudinal magnetic fields. However, in case of a centred dipole where both poles come alternatively into view as the star rotates, we should also expect the modulus variation curve to appear as a perfect double wave, that is, we would see a sinusoid with twice the rotation frequency of the star. From the simultaneous consideration of the phase curves of variation of the longitudinal field and of the mean field modulus based on a more complete observational dataset, it will become possible to better constrain the magnetic field structure (e.g., dipole offset along its axis or superposition of dipole, quadrupole, and octupole components).

Acknowledgements. We thank the referee G. Mathys for constructive comments that helped us to improve the paper. Funding for the Sloan Digital Sky Survey V has been provided by the Alfred P. Sloan Foundation, the Heising-Simons Foundation, the National Science Foundation, and the Participating Institutions. SDSS acknowledges support and resources from the Center for High-Performance Computing at the University of Utah. SDSS telescopes are located at Apache Point Observatory, funded by the Astrophysical Research Consortium and operated by New Mexico State University, and at Las Campanas Observatory, operated by the Carnegie Institution for Science. The SDSS web site is www.sdss.org. SDSS is managed by the Astrophysical Research Consortium for the Participating Institutions of the SDSS Collaboration, including Caltech, The Carnegie Institution for Science, Chilean National Time Allocation Committee (CNTAC) ratified researchers, The Flatiron Institute, the Gotham Participation Group, Harvard University, Heidelberg University, The Johns Hopkins University, L'Ecole polytechnique fédérale de Lausanne (EPFL), Leibniz-Institut für Astrophysik Potsdam (AIP), Max-Planck-Institut für Astronomie (MPIA Heidelberg), Max-Planck-Institut für Extraterrestrische Physik (MPE), Nanjing University, National Astronomical Observatories of China (NAOC), New Mexico State University, The Ohio State University, Pennsylvania State University, Smithsonian Astrophysical Observatory, Space Telescope Science Institute (STScI), the Stellar Astrophysics Participation Group, Universidad Nacional Autónoma de México, University of Arizona, University of Colorado Boulder, University of Illinois at Urbana-Champaign, University of Toronto, University of Utah, University of Virginia, Yale University, and Yunnan University. Based on observations made with ESO Telescope at the La Silla Observatory under programme IDs 0108.D-0205(B) and 0109.C-0265(A). This work has made use of data from the European Space Agency (ESA) mission *Gaia* (<https://www.cosmos.esa.int/gaia>), processed by the *Gaia* Data Processing and Analysis Consortium (DPAC, <https://www.cosmos.esa.int/web/gaia/dpac/consortium>). Funding for the DPAC has been provided by national institutions, in particular the institutions participating in the *Gaia* Multilateral Agreement. This work has made use of the VALD, operated at Uppsala University, the Institute of Astronomy RAS in Moscow, and the University of Vienna.

References

- Ahumada, R., Prieto, C. A., Almeida, A., et al. 2020, *ApJS*, 249, 3
 Asplund, M., Amarsi, A. M., & Grevesse, N. 2021, *A&A*, 653, A141
 Babcock, H. W. 1958, *ApJ*, 128, 228
 Babcock, H. W. 1960, *ApJ*, 132, 521
 Bernhard, K., Hümmerich, S., Otero, S., & Paunzen, E. 2015, *A&A*, 581, A138
 Brasseur, C. E., Phillip, C., Fleming, S. W., Mullally, S. E., & White, R. L. 2019, *Astrocut: Tools for creating cutouts of TESS images*
 Chojnowski, S. D., Hubrig, S., Hasselquist, S., et al. 2020, *MNRAS*, 496, 832
 Chojnowski, S. D., Hubrig, S., Hasselquist, S., et al. 2019, *ApJ*, 873, L5
 Chojnowski, S. D., Hubrig, S., Labadie-Bartz, J., et al. 2022, *MNRAS*, 516, 2812
 Chojnowski, S. D., Hubrig, S., Nidever, D. L., et al. 2023, *MNRAS*, 522, 5931
 Claret, A. 2019, *Research Notes of the American Astronomical Society*, 3, 17
 Cowley, C. R., Allen, M. S., & Aikman, G. C. L. 1975, *Nature*, 258, 311
 Donati, J. F., Semel, M., Carter, B. D., Rees, D. E., & Collier Cameron, A. 1997, *MNRAS*, 291, 658

- Donati, J. F., Semel, M., & Rees, D. E. 1992, *A&A*, 265, 669
- Elkin, V. G., Kurtz, D. W., & Nitschelm, C. 2012, *MNRAS*, 420, 2727
- Fabricsius, C., Høg, E., Makarov, V. V., et al. 2002, *A&A*, 384, 180
- Gaia Collaboration, Prusti, T., de Bruijne, J. H. J., et al. 2016, *A&A*, 595, A1
- Gaia Collaboration, Vallenari, A., Brown, A. G. A., et al. 2022, arXiv e-prints, arXiv:2208.00211
- Ghazaryan, S., Alecian, G., & Hakobyan, A. A. 2018, *MNRAS*, 480, 2953
- Giarrusso, M., Cecconi, M., Cosentino, R., et al. 2022, *MNRAS*, 514, 3485
- Gunn, J. E., Siegmund, W. A., Mannery, E. J., et al. 2006, *AJ*, 131, 2332
- Hubrig, S., Ilyin, I., Schöller, M., & Lo Curto, G. 2013, *Astronomische Nachrichten*, 334, 1093
- Hubrig, S., Järvinen, S. P., Madej, J., et al. 2018, *MNRAS*, 477, 3791
- Hubrig, S., Kurtz, D. W., Bagnulo, S., et al. 2004a, *A&A*, 415, 661
- Hubrig, S., Szeifert, T., Schöller, M., Mathys, G., & Kurtz, D. W. 2004b, *A&A*, 415, 685
- Jagelka, M., Mikulášek, Z., Hümmerich, S., & Paunzen, E. 2019, *A&A*, 622, A199
- Järvinen, S. P., Hubrig, S., Mathys, G., et al. 2020, *MNRAS*, 499, 2734
- Jarzębowski, T. 1960, *Acta Astron.*, 10, 119
- Kupka, F., Dubernet, M. L., & VAMDC Collaboration. 2011, *Baltic Astronomy*, 20, 503
- Kurucz, R. L. 2005, *Memorie della Societa Astronomica Italiana Supplementi*, 8, 14
- Lenz, P. & Breger, M. 2005, *CoAst*, 146, 53
- Lightkurve Collaboration, Cardoso, J. V. d. M., Hedges, C., et al. 2018, *Lightkurve: Kepler and TESS time series analysis in Python*, *Astrophysics Source Code Library*
- Majewski, S. R., Schiavon, R. P., Frinchaboy, P. M., et al. 2017, *AJ*, 154, 94
- Mathys, G. 1989, *Fund. Cosmic Phys.*, 13, 143
- Mathys, G. 1990a, *A&A*, 232, 151
- Mathys, G. 1990b, *A&A*, 236, 527
- Mathys, G. 2017, *A&A*, 601, A14
- Mathys, G., Hubrig, S., Landstreet, J. D., Lanz, T., & Manfroid, J. 1997, *A&AS*, 123, 353
- Mathys, G. & Lanz, T. 1992, *A&A*, 256, 169
- Mathys, G., Romanyuk, I. I., Hubrig, S., et al. 2019, *A&A*, 624, A32
- Mayor, M., Pepe, F., Queloz, D., et al. 2003, *The Messenger*, 114, 20
- Nidever, D. L., Holtzman, J. A., Allende Prieto, C., et al. 2015, *AJ*, 150, 173
- Pepe, F., Mayor, M., Delabre, B., et al. 2000, in *Society of Photo-Optical Instrumentation Engineers (SPIE) Conference Series*, Vol. 4008, *Optical and IR Telescope Instrumentation and Detectors*, ed. M. Iye & A. F. Moorwood, 582–592
- Preston, G. W. 1967, *ApJ*, 150, 547
- Preston, G. W. 1969, *ApJ*, 156, 967
- Przybylski, A. 1961, *Nature*, 189, 739
- Renson, P. & Manfroid, J. 2009, *A&A*, 498, 961
- Ricker, G. R., Winn, J. N., Vanderspek, R., et al. 2015, *Journal of Astronomical Telescopes, Instruments, and Systems*, 1, 014003
- Schneider, F. R. N., Ohlmann, S. T., Podsiadlowski, P., et al. 2020, *MNRAS*, 495, 2796
- Schöller, M., Hubrig, S., Fossati, L., et al. 2017, *A&A*, 599, A66
- Scholz, G. 1978, *Astronomische Nachrichten*, 299, 81
- Stibbs, D. W. N. 1950, *MNRAS*, 110, 395
- Wilson, J. C., Hearty, F. R., Skrutskie, M. F., et al. 2019, *PASP*, 131, 055001

Appendix A: Longitudinal magnetic field measurements using HARPS spectropolarimetric observations

The measured mean longitudinal magnetic field strengths for all line masks are presented in Table A.1.

LSD Stokes I , and V profiles calculated for the separate masks with Ti II, Cr II, Fe II, and Sr II, are presented in Fig. A.1. The results of the LSD technique applied for the lines masks constructed for rare earth elements Nd III, Dy III, and Er III are presented in Fig. A.2. The comparison between Stokes I and V profiles calculated for once and twice ionised Si lines is shown in Fig. A.3. As diagnostic null spectra for all measurements appear flat and featureless, they are not presented in these figures. The dashed lines in Stokes V panels indicate the mean uncertainty, which in numerous cases is not larger than the thickness of these lines.

Table A.1. LSD mean longitudinal magnetic field measurements for different line masks.

Mask	\bar{g}_{eff}	$\langle B_z \rangle$ (kG)	$\langle B_z \rangle$ (kG)	$\langle B_z \rangle$ (kG)	$\langle B_z \rangle$ (kG)	$\langle B_z \rangle$ (kG)	$\langle B_z \rangle$ (kG)	$\langle B_z \rangle$ (kG)	$\langle B_z \rangle$ (kG)
φ_{rot}		0.046	0.179	0.288	0.305	0.415	0.540	0.793	0.923
All (87)	1.14	-3.32 ± 0.09	-1.43 ± 0.08	0.64 ± 0.06	0.79 ± 0.06	1.43 ± 0.04	1.43 ± 0.04	-1.73 ± 0.06	-3.22 ± 0.10
Ti II (10)	1.08	-3.66 ± 0.21	-1.74 ± 0.16	1.00 ± 0.12	0.99 ± 0.12	1.55 ± 0.09	1.82 ± 0.08	-1.61 ± 0.20	-3.68 ± 0.18
Cr II (9)	1.05	-3.62 ± 0.21	-1.56 ± 0.25	0.58 ± 0.13	0.44 ± 0.16	1.63 ± 0.13	1.56 ± 0.13	-1.71 ± 0.13	-3.50 ± 0.23
Fe II (22)	1.04	-3.38 ± 0.20	-1.58 ± 0.16	0.69 ± 0.10	0.78 ± 0.12	1.53 ± 0.07	1.58 ± 0.09	-1.49 ± 0.13	-3.46 ± 0.18
Sr II (3)	1.20	-2.51 ± 0.43	-1.75 ± 0.30	1.55 ± 0.13	0.78 ± 0.19	1.12 ± 0.11	0.93 ± 0.13	-2.27 ± 0.24	-2.81 ± 0.28
Nd III (14)	1.18	-4.30 ± 0.27	-1.80 ± 0.23	0.50 ± 0.16	1.59 ± 0.12	1.38 ± 0.12	1.43 ± 0.12	-1.48 ± 0.13	-4.17 ± 0.21
Dy III (11)	1.15	-5.34 ± 0.53	-1.56 ± 0.41	1.00 ± 0.26	0.99 ± 0.22	0.83 ± 0.23	1.16 ± 0.23	-2.63 ± 0.34	-5.56 ± 0.40
Er III (5)	1.18	-3.96 ± 0.93	-2.48 ± 0.56	1.95 ± 0.28	1.42 ± 0.27	1.58 ± 0.27	1.36 ± 0.22	-1.67 ± 0.38	-4.09 ± 0.67
Si II (10)	1.19	-2.98 ± 0.12	-0.60 ± 0.06	0.63 ± 0.04	0.76 ± 0.04	1.08 ± 0.03	1.13 ± 0.05	-1.17 ± 0.05	-3.26 ± 0.15
Si III (3)	1.83	-2.24 ± 0.10	-1.04 ± 0.08	0.37 ± 0.08	0.64 ± 0.07	0.92 ± 0.05	0.87 ± 0.08	-1.15 ± 0.08	-2.28 ± 0.09

Notes: In the first column we present the number of lines used in each mask followed by the average Landé factors and the field measurements in kG. All measurements are definite detections.

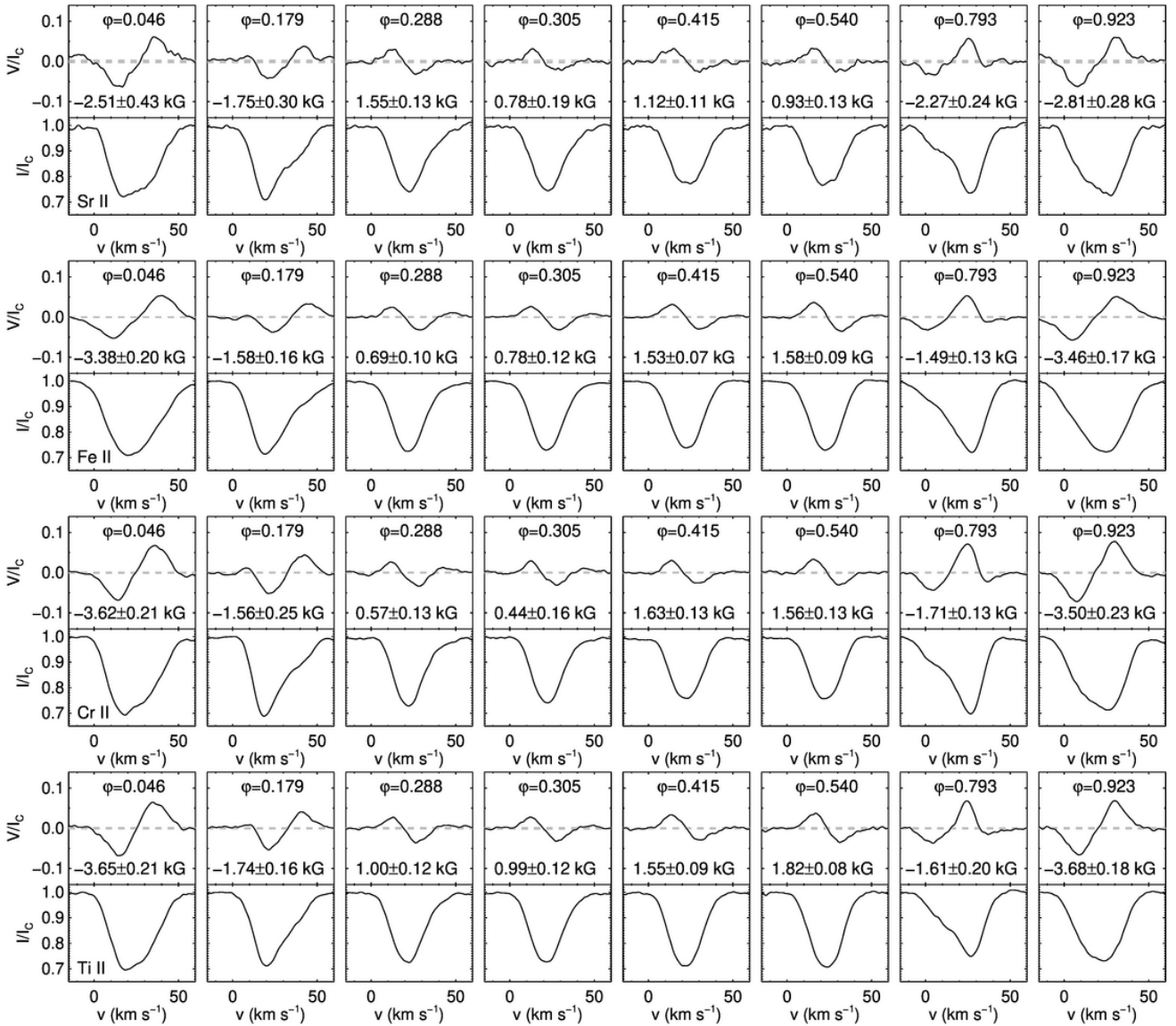


Fig. A.1. Four panels present HARPS LSD Stokes *I* and Stokes *V* spectra of HD 57372 employing line masks with Sr II, Ti II, Cr II, Fe II lines, and ionSrii lines. The dashed lines in the Stokes *V* panels indicate the mean uncertainties, which for the presented line masks are of the order of the thickness of these lines.

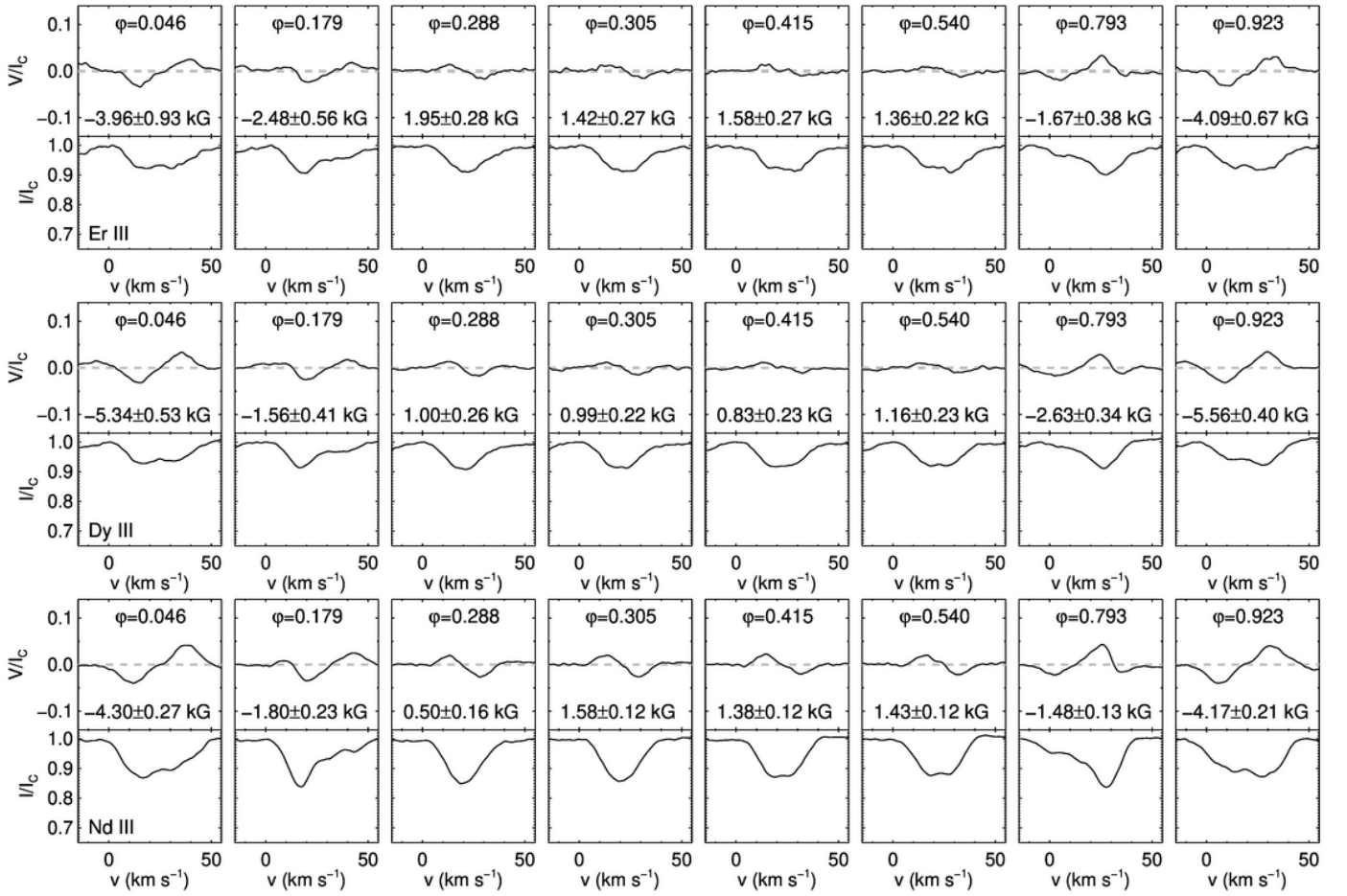


Fig. A.2. As Fig. A.1, but for REEs Nd III, Dy III, and Er III.

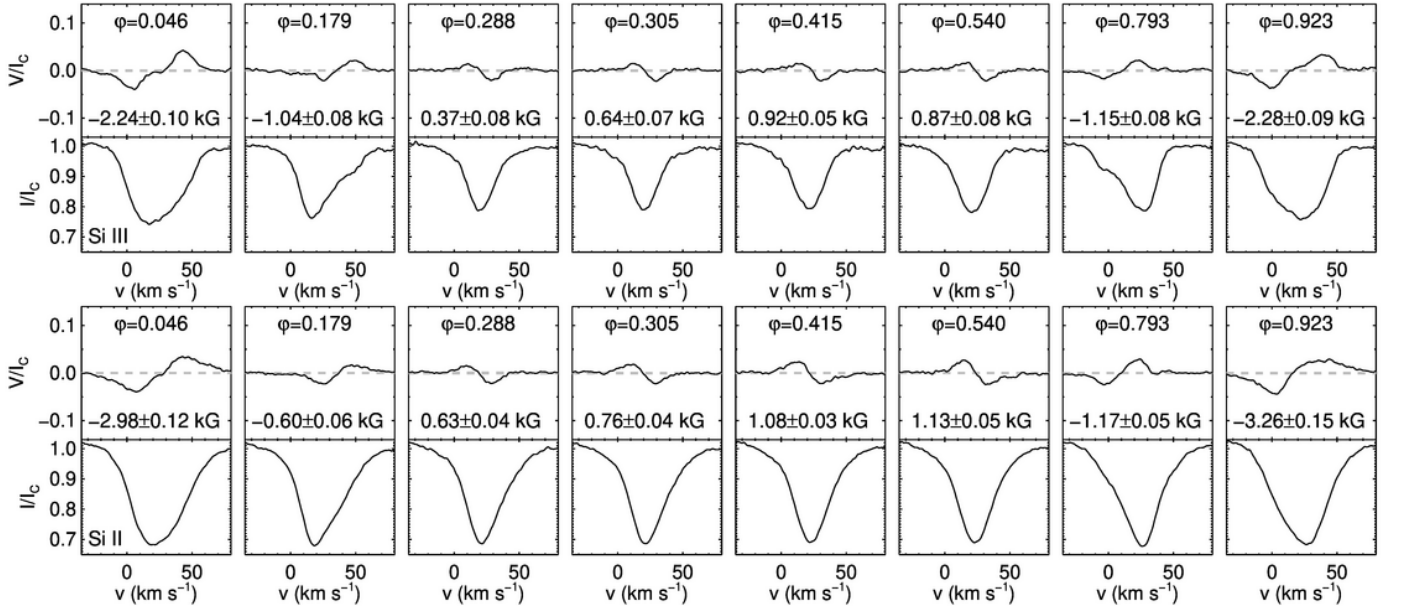


Fig. A.3. As Fig. A.1, but for Si II and Si III.